Eur. Phys. J. B **15**, 41–50 (2000)

THE EUROPEAN PHYSICAL JOURNAL B

EDP Sciences
© Società Italiana di Fisica
Springer-Verlag 2000

Evidence of bcc Mn epitaxial growth in $Mn/M_xV_{1-x}(001)$ (M = Fe, Nb) superlattices

P.Y. Friot[1], P. Turban[1], S. Andrieu[1,a], M. Piecuch[1], E. Snoeck[2], A. Traverse[3], E. Foy[3], and C. Theodorescu[3]

[1] Laboratoire de Physique des Matériaux, CNRS/Université Nancy I, BP 239, 54506 Vandœuvre-les-Nancy Cedex, France
[2] CEMES/LOE, CNRS, BP 4347, 31055 Toulouse, France
[3] LURE, CNRS/CEA/Université Paris-Sud, BP 34, 91898 Orsay, France

Received 21 June 1999

Abstract. This study is dedicated to the growth of bcc Mn by molecular beam epitaxy, in order to look at the magnetic properties of bcc Mn near room temperature. For this purpose, Mn is deposited on bcc $M_xV_{1-x}(001)$ alloy lattices (M = Fe or Nb) for which the lattice spacing is tunable by varying the concentration x. We first show that the parameter of the M_xV_{1-x} alloy's buffer layers can be adjusted from 2.95 Å to 3.3 Å depending on x and M. Three different structures in Mn films grown on these buffer layers are observed depending on the in-plane spacing of the initial M_xV_{1-x} lattice. Thick Mn films are always found to grow epitaxially in the Mnα structure. For moderate thicknesses larger than 4 atomic planes, Mn grows in an unidentified structure. Finally, up to four deposited atomic planes, Mn is found to grow in a tetragonal structure close to a bcc one on Fe(001), $Fe_xV_{1-x}(001)$ and $Nb_xV_{1-x}(001)$ for $x \leq 25\%$. This tetragonal structure is shown to be a distorsion of a Mn bcc structure with $a = 2.92$ Å. Except for ultra-thin Mn films deposited on Fe(001), no macroscopic magnetization is detected in our strained bcc Mn samples. These results are compared to theoretical predictions.

PACS. 68.55.-a Thin film structure and morphology – 68.65.+g Low-dimensional structures (superlattices, quantum well structures, multilayers): structure, and nonelectronic properties – 75.70.-i Magnetic films and multilayers

1 Introduction

The 3*d* elements of the first transition series are different from the other transition metals because of their magnetic behaviour. The occurrence of magnetism in these transition metals, as proposed by Stoner, is to be associated with the high density of states at the Fermi level. This condition is fulfilled in 3*d* transition metals for which the 3*d* shell is only partly occupied. A magnetic ground state is actually observed in Cr, Mn, Fe, Co and Ni. However, whereas Fe, Co and Ni naturally exist in a ferromagnetic state, Cr and Mn are in an antiferromagnetic state. This last magnetic arrangement is favoured compared to the ferromagnetic order when the *d*-shell is half-filled. Nevertheless, the magnetic properties of these 3*d* elements also depend on the atomic volume. In general, magnetic ordering is predicted for large atomic volume, whereas for small atomic volume the ground state is found to be non-magnetic [1]. Various magnetic orderings are predicted for intermediate atomic volumes. For the verification of these theoretical predictions, however, these materials need to be prepared in strained or metastable structures near room temperature. The molecular beam epitaxy technique is a powerful tool for this purpose since pseudomorphic epitaxy is often observed in the early growth stage. Highly strained or metastable structures can sometimes be epitaxially grown on an appropriate buffer layer. For instance, iron (under ambient conditions) can be prepared in its allotropic fcc structure (stable at high temperature) at room temperature on (001) Cu [2]. The case of Mn is interesting because of its natural tendency to be in an antiferromagnetic state. Preparing Mn in a structure for which a ferromagnetic ordering takes place is consequently a challenge.

The magnetic properties of bulk fcc and bcc Mn in a large atomic volume range have been theoretically studied by several authors [1,3–6]. In fcc Mn, only two magnetic states are stable [3]. A non-magnetic to antiferromagnetic transition is predicted when increasing the atomic volume. In the case of bcc Mn, a third magnetic state is predicted in the magnetic phase diagram [4,5]. When increasing the atomic volume, non-magnetic, ferri- [4] or ferro-magnetic [5] and antiferromagnetic states are successively found to be the ground magnetic state. From the experimental point of view, a Mn pseudomorphic growth up to several atomic planes was observed on various surfaces, like Ru and Ni [7], Al [8], Pd [9], Cu and Ag [10], fcc Co [11] and hcp Co [12], Ir [13] Fe [14] and V [15].

[a] e-mail: andrieu@lpm.u-nancy.fr

Table 1. Mn structures: stability with temperature and corresponding lattice spacings.

temperature (K)	structures	lattice spacing (Å)
300–751	Mnα	8.914
752–1094	Mnβ	6.315
1095–1133	fcc	3.862
1134–1245	bcc	3.081

Except on Fe and V(001), the Mn structure is always found to derive from the fcc structure (tri- or tetragonalized). No macroscopic magnetization was detected in these new Mn structures. In the case of the ferromagnetic Fe buffer layer, a Mn tetragonal structure was found [14–16] but Kim *et al.* [15,16] showed that it may be derived from both bcc or fcc Mn. On Fe(001), a Mn magnetic ordering is observed on the first planes [14], which vanishes when the ultra-thin Mn films are coated by Fe, or when the Mn thickness is increased. The situation is quite similar for Mn ultra- thin films deposited on fcc Co [11]. To our knowledge, the Mn/V(001) magnetic properties have not been investigated yet. Concluding this section, these results indicate that no ferromagnetic ordering takes place in "bulk" Mn fcc or strained fcc films. This is in agreement with theoretical studies dedicated to fcc Mn [3]. However, as the bcc Mn growth near room temperature by MBE has never been clearly demonstrated up to now, nothing can be said about any ferro- or ferri-magnetic ordering in such a Mn structure. The goal of this study is to grow Mn in a bcc structure and to determine its magnetic properties.

Why is this bcc Mn structure so difficult to obtain by epitaxy? In order to answer this question, an analysis of the stability of the different Mn crystallographic structures is necessary. Under regular conditions of pressure and without any stress, Mn adopts several crystallographic structures when increasing the temperature, as listed in Table 1. In the case of Mn epitaxy on a buffer layer, this Mn phase diagram is modified by the stress induced by the mismatch between Mn and the buffer layer. Indeed, the in-plane stress due to the buffer layer plays the role of pressure and the resulting elastic energy has to be added to the cohesive energy of these structures. The high temperature fcc and bcc structures may thus be grown near room temperature. However, for a fixed in-plane stress, the fcc structure is more stable than the bcc one. In order to favour the bcc structure, the mismatch between the lattice parameters of the Mn bcc and the buffer layer must be very small. In that case, the mismatch between the Mn fcc and the buffer layer is large, as well as the resulting elastic energy. A large elastic energy for the fcc structure and a close to zero one for the bcc structure can lead to a lower total energy for the bcc than for the fcc structure. Moreover, the Mnα and Mnβ lattice spacings are near twice and triple the parameter of bcc Mn, respectively (see Tab. 1). This is another difficulty to achieve the bcc Mn epitaxy. For all these reasons, a necessary condition to grow bcc Mn is to choose a buffer layer with a parameter close to the bcc Mn lattice spacing.

The bcc Mn lattice spacing is known only at high temperatures (3.08 Å) but not near room temperature (temperature of epitaxy). A solution is to grow a buffer layer with a tunable lattice spacing. This can be achieved by growing XY alloys, with the condition that X and Y are totally miscible. The phase diagrams of the binary alloys show that this condition is fulfilled for Fe_xV_{1-x} alloys with $x \leq 25\%$ and for Nb_xV_{1-x} alloys with $0 \leq x \leq 1$. The buffer layer lattice parameter can thus theoretically vary from 2.99 Å ($Fe_{0.25}V_{0.75}$) to 3.30 Å (Nb) with x.

The Mn epitaxial relation with $M_xV_{1-x}(001)$ lattice is analysed during the growth by RHEED. The chemical quality of the deposits as well as the interdiffusion between Mn and the buffer layers are monitored by Auger electron and X-ray photoemission spectroscopies. The morphology of Mn/M_xV_{1-x} superlattices is examinated by transmission electron microscopy. The structure of Mn and M_xV_{1-x} are determined by $\theta - 2\theta$ X-ray diffraction and X-ray absorption spectroscopy (EXAFS). Finally, the Mn magnetic properties are analysed by X-ray magnetic circular dichroism and SQUID measurements.

2 Experimental set up

The M_xV_{1-x} and Mn films were grown in a Molecular Beam Epitaxy chamber in which a pressure of 3.5×10^{-11} hPa (2×10^{-11} torr) is obtained after the cryogenic panels are cooled with liquid nitrogen. V and Nb were evaporated at typical growth rates around 1 Å/s by using electron guns. Mn and Fe are sublimed by using Knudsen cells, leading to growth rates from 1 to 10 Å/min. A PBN crucible was used to sublime Mn in order to avoid any oxygen contamination. 1000 Å thick (001) M_xV_{1-x} buffer layers are grown at 1100 K on (001) MgO substrates. The Mn films were grown on these alloy buffer layers for substrate temperatures in the range of 300 to 1000 K.

The chemical analysis was performed by using both Auger electron and X-ray photoemission spectroscopies (AES and XPS). The Fe and Nb concentrations (x) were adjusted by controlling the growth rate of Fe, V and Nb measured with a quartz microbalance located at the position of the sample. The concentration x in the alloys was verified by XPS. The primary energy of the AES electron beam was 3 kV. The angle between the sample and the AES and XPS electron detector was 20°. No C contamination was detected on Mn and M_xV_{1-x} films. The oxygen contamination of M_xV_{1-x} films cannot be quantitatively determined by AES or XPS, since V is one of the few elements for which the Auger O KLL and V LMM peaks and the photoelectron O 1s and V 2p peaks overlap. Despite the very small base pressure in the MBE chamber, some oxygen contamination was detected by XPS (see Fig. 1), due to the large oxidation enthalpies of V and Nb. This oxygen contamination could be a problem for our purpose since the Mn magnetic properties can be strongly affected. However, no oxygen contamination was detected on Mn films by XPS. Moreover, the EXAFS analysis does

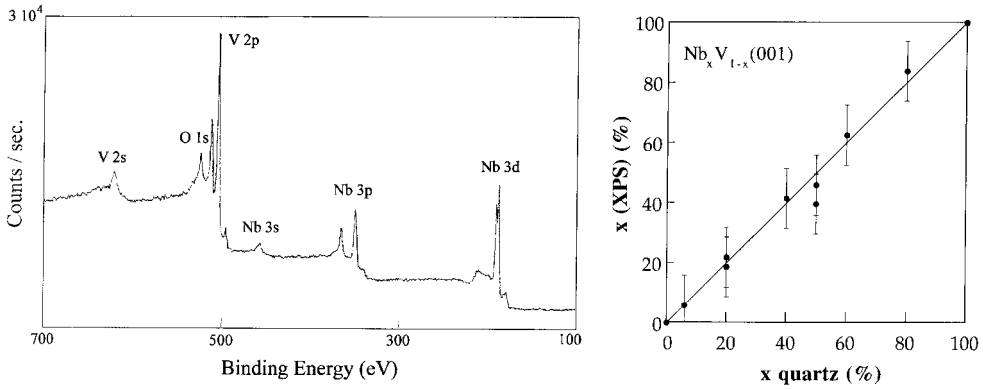

Fig. 1. XPS spectrum example obtained on a 1000 Å thick $Nb_{0.5}V_{0.5}$ (001) buffer layer (left), and comparison between the Nb concentrations determined by XPS and quartz calibration (right).

not provide evidence for any manganese oxide phase. The possible influence of this small oxygen contamination on the Mn magnetic properties is discussed in the last part of the paper.

The morphology and crystallographic structure of the films and superlattices were determined by using RHEED, high resolution electron transmission microscopy (HRTEM), $\theta - 2\theta$ X-ray diffraction (XRD) and EXAFS. The energy of the incident electron beam used in the RHEED experiments was 30 kV, leading to a wavelength of 0.07 Å. The high resolution electron transmission microscopy (HRTEM) experiments were performed on a Philips CM30/ST working at 300 kV, with a resolution of 1.9 Å. The images were calibrated using the lattice spacing of the MgO substrate. The EXAFS data collection was carried out at 77 K on the D42 station of the DCI ring (LURE) at the V, Mn, Fe and Nb K-edges (5465, 6539, 7112 and 18 986 eV, respectively). The total electron yield technique was used. The EXAFS spectra were carried out using two geometries, *i.e.* with the samples oriented parallel or perpendicular to the X-ray beam's linear polarization. This is of particular interest in the case of a non-cubic structure. The EXAFS oscillations were simulated by using the FEFF7 code for which the multiple scattering process is taken into account.

Finally, the magnetic behaviour was examinated by using *in situ* X-ray magnetic circular dichroïsm (XMCD) performed on uncapped Mn films, and by SQUID performed on superlattices. The XMCD measurements were performed at 100 K for an applied magnetic field up to 1 T. More experimental details about XMCD measurements are given in reference [14]. The SQUID measurements were performed with an applied magnetic field from 0 to 7 T, in the temperature range 4.2–400 K.

3 Experimental results

3.1 Structure and lattice parameter of M_xV_{1-x} alloys

First of all, the relation between the concentration x and the growth rates has to be examined. The concentration x is given by the ratio of the impinging flux of species M, F_M, with the total impinging flux $F_M + F_V$. Moreover, the flux F_i measured on the quartz microbalance is equal to the growth rate v_i multiplied by the density ρ_i of the material in its regular structure. As Fe, V and Nb are bcc, the densities are equal to $2/a_i^3$, and we finally get the relation between x and the growth rates as:

$$x = \frac{F_M}{F_M + F_V} = \frac{1}{1 + \dfrac{\rho_V v_V}{\rho_M v_M}} = \frac{1}{1 + \left(\dfrac{a_M}{a_V}\right)^3 \dfrac{v_V}{v_M}} \cdot \quad (1)$$

This trivial calculation shows that the concentration x is not equal to the ratio of the M growth rate to the total growth rate. Indeed, $(a_{Nb}/a_V)^3 = 1.29$ and $(a_{Fe}/a_V)^3 = 0.90$. In this study, the Fe growth rate was fixed to 5 Å/min, and the Nb one to 0.5 Å/s. A given concentration x was obtained by adjusting the vanadium growth rate using equation (1).

When binary alloys are grown, there is some possibility that one of the materials segregates on top of the growing layer. In order to investigate this point, we have performed XPS measurements in order to determine the x concentration near the surface. According to reference [17], the ratio of the XPS intensity peaks is roughly equal to:

$$\frac{I_M}{I_V} = \frac{\sigma_M}{\sigma_V} \left(\frac{x}{1-x}\right) \sqrt{\frac{E_V}{E_M}} \quad (2)$$

were σ_i are the absorption cross-sections [18] and E_i the energies of the photoelectrons. The x determination was performed by analysing the photoelectrons coming from the V $2p$, Fe $2p$ and Nb $3p$ core levels (using the Mg anode). As the corresponding kinetic energies are close to 700 eV, we can roughly estimate that we analysed the upper 10 monolayers. The x values determined by this technique are not very accurate but this allows us to detect any strong segregation phenomenon. As shown in Figure 1, the x values determined by XPS and quartz microbalance measurements are in good agreement. This means that if some segregation phenomenon exists, it is limited and not a problem for our purpose.

For all concentrations of x employed here, the RHEED patterns observed on the alloys surface are typical of a square lattice rotated by 45° with respect to the (001) MgO lattice, as shown in Figure 2. Whereas superstructures were observed on pure V and Nb buffer

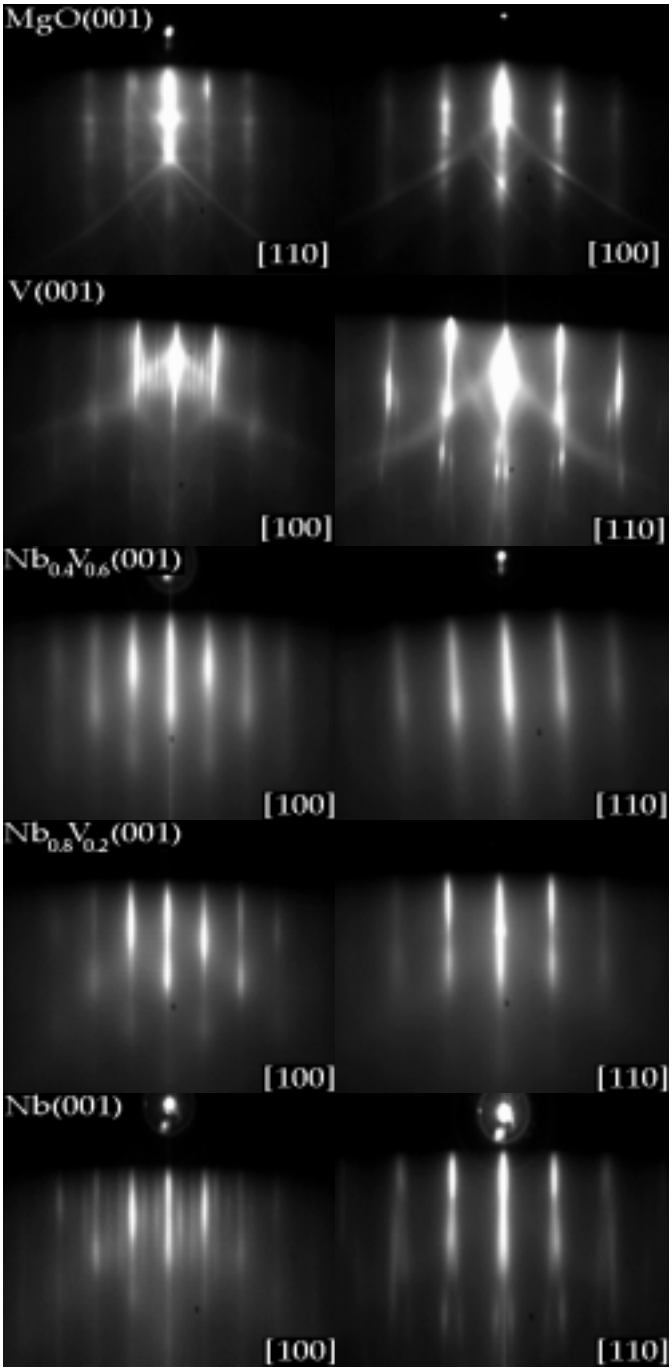

Fig. 2. RHEED patterns observed on the Nb_xV_{1-x} buffer layers grown on MgO. The epitaxial relation is NbV(001) ∥ MgO(001) and NbV[100] ∥ MgO[110]. Surface superstructures are observed on pure V and Nb buffer layers but not on the alloys. The azimuths denoted on the RHEED patterns give the crystallographic directions of the deposits.

layers' surfaces, no reconstruction was observed on the alloys. These superstructures are often attributed to oxygen contamination [19]. It should be noted however that no such surface reconstruction was observed during the superlattices growth. We consequently assume that this oxygen contamination is due to the high temperature needed to grow buffer layers with flat surfaces. The RHEED analysis shows that the in-plane lattice parameters of the buffer layers are close to the lattice parameters of NbV alloys. The out-of-plane lattice parameters determined by X-ray diffraction experiments performed in the $\theta - 2\theta$ mode on 1000 Å thick buffer layers is observed to follow Vegard's law (Fig. 3):

$$a_{\text{alloy}} = x a_{\text{Nb}} + (1-x) a_{\text{V}} = a_{\text{V}} + (a_{\text{Nb}} - a_{\text{V}})x \qquad (3)$$

where a_{Nb} and a_{V} are the lattice spacings of bulk V and Nb, respectively. This confirms that the materials are totally miscible, and that the alloys keep the bcc structure. This result is also confirmed by EXAFS. A similar study was performed for Fe_xV_{1-x} alloys with $x = 12\%$ and 25%. The epitaxial relation is similar to the NbV/MgO(001) system, and the lattice parameter is found to be 2.95 Å for $x = 25\%$ and 2.99 Å for $x = 12\%$. In summary, we have verified that bcc Fe_xV_{1-x} and Nb_xV_{1-x} alloy buffer layers can be grown on MgO(001) with the epitaxial relation: MV(001) ∥ MgO(001) and MV[100] ∥ MgO[110]. A tunable parameter from 2.95 to 3.3 Å is obtained. This study augments our previous results obtained on the Mn/Fe(001) system, for which the Fe buffer layer lattice spacing is 2.87 Å [14].

3.2 Mn growth on M_xV_{1-x}(001) alloys

The Mn interdiffusion in the M_xV_{1-x} alloys was studied by AES. A four monolayer (ML) thick Mn film was first grown at room temperature on the (001) alloys lattice. The temperature at which the interdiffusion becomes noticeable was determined by measuring the variation of the Auger $I_{\text{Mn}}/I_{\text{V}}$ peaks ratio when the substrate temperature was increased from 300 to 1100 K. I_{Mn} is the intensity of the Mn LMM Auger peak at 589 eV and I_{V} is the intensity of the V LMM Auger peak at 473 eV. A decrease of the Auger $I_{\text{Mn}}/I_{\text{V}}$ peak ratio was clearly observed above 750 K, which can be due to the occurrence of interdiffusion (Fig. 4). However, this may also be due to the Mn desorption from the surface since the Mn vapour pressure is not negligible at this temperature. This hypothesis is supported by the fact that Mn is totally eliminated from the surface when increasing the temperature up to 1100 K.

Because of these findings, the Mn growth was essentially studied for substrate temperatures in the range 300–600 K. Several RHEED patterns were observed depending on the buffer layer characteristics (M and x) and on the Mn film thickness (Fig. 5). For thick Mn films, and independent of the buffer alloy, clear RHEED patterns corresponding to a reciprocal lattice three times smaller than the M_xV_{1-x} (001) lattice were observed (Fig. 5c). This means that the in-plane Mn parameter is near 9 Å, which has to be compared to the Mnα lattice spacing equal to 8.91 Å. For thinner Mn films, two other structures were observed. First, a complex and diffuse surface structure is obtained on Nb_xV_{1-x} buffer alloys with $x > 25\%$. This surface structure is also observed on Fe_xV_{1-x} and Nb_xV_{1-x} alloys with $x < 25\%$ but for Mn thicknesses larger than four monolayers (Fig. 5b).

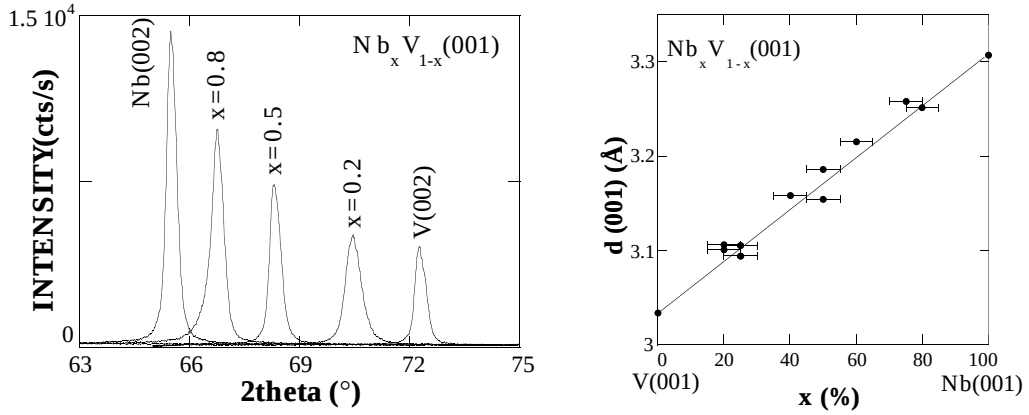

Fig. 3. Example of $\theta - 2\theta$ X-ray diffraction diagrams obtained on a series of 1000 Å thick Nb_xV_{1-x} (001) buffer layers (left). From the XRD spectra, the variation of the (001) lattice spacing with the Nb concentration x is deduced (right).

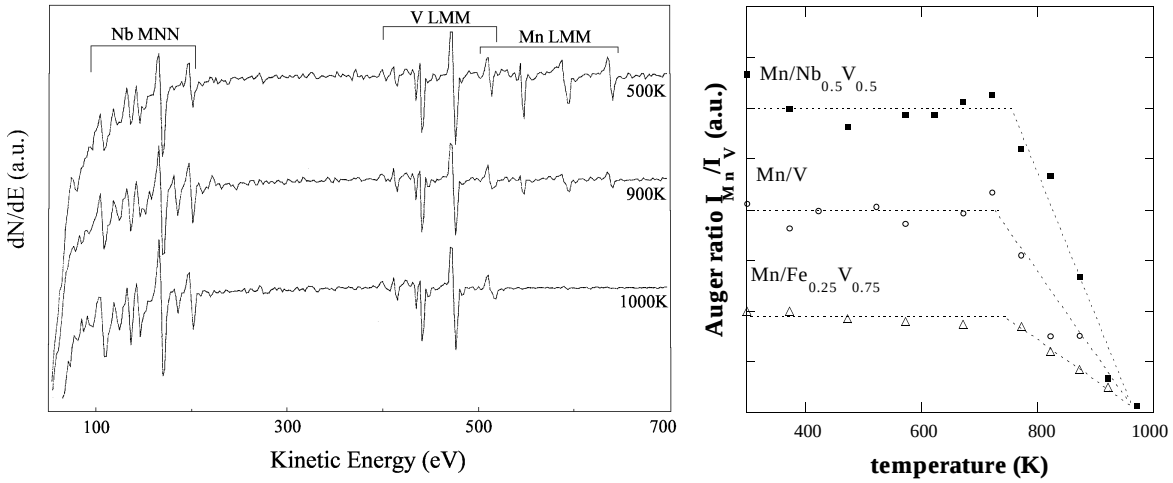

Fig. 4. Examples of Auger spectra obtained on a 4 ML $Mn/Nb_{0.5}V_{0.5}$ (001) sample for several annealing temperatures (left) and corresponding variation of the Auger peak ratio $I_{Mn}(589\text{ eV})/I_V(473\text{ eV})$ with the annealing temperature. The Mn interdiffusion (or desorption) is clearly observed above 750 K.

But the most interesting result was obtained for Mn films up to four monolayers thick deposited on Fe_xV_{1-x} and Nb_xV_{1-x} alloys with $x < 25\%$. The Mn surface lattice is observed to match the initial square lattice of the buffer layer (Figs. 2 and 5a). This pseudomorphic regime can be explained by the growth of bcc Mn. However, as the three-dimensional structure cannot be unambiguously determined by RHEED, then XRD and EXAFS analyses were performed.

3.3 Three-dimensional Mn structures

In order to have a sufficient amount of material for a structural analysis, Mn/M_xV_{1-x} superlattices (SLs) were grown. However, the quality of the Mn and MV layers stacking has to be checked. For this purpose, a HRTEM study was performed on two superlattices with the stacking sequence $(Mn(6\text{ Å})/Fe_{0.25}V_{0.75}(17\text{ Å})) \times 100$ and $(Mn(6\text{ Å})/Nb_{0.25}V_{0.75}(24\text{ Å})) \times 100$ (Fig. 6). Despite the very small contrast of the elements in these superlattices, the stacking sequence is clearly visible, which is another indication of the lack of interdiffusion. Moreover, the HRTEM images demonstrate that the interfaces are flat on a large scale.

The diffraction diagram of a $(A/B) \times N$ superlattice with a superperiod of Λ consists of a series of peaks separated by $2\pi/\Lambda$, modulated by the structure factor of the supercell. When the A and B out-of-plane lattice spacings d_A and d_B are similar, the structure factor is centered around these lattice spacings. In this case, the most intense peak of the superlattice corresponds to the average of these lattice spacings $\langle d \rangle = (n_A d_A + n_B d_B)/(n_A + n_B)$ (n_A and n_B denote the number of A and B planes). This peak is often called the superlattice peak and the other satellite peaks. If d_A is close to d_B, the superlattice peak should be close to the diffracted peak coming from the buffer layer B. The $\theta - 2\theta$ XRD diagrams measured on pseudomorphic Mn-based superlattices (Figs. 7a–c) actually exhibit superlattice peaks (denoted $n = 0$) close

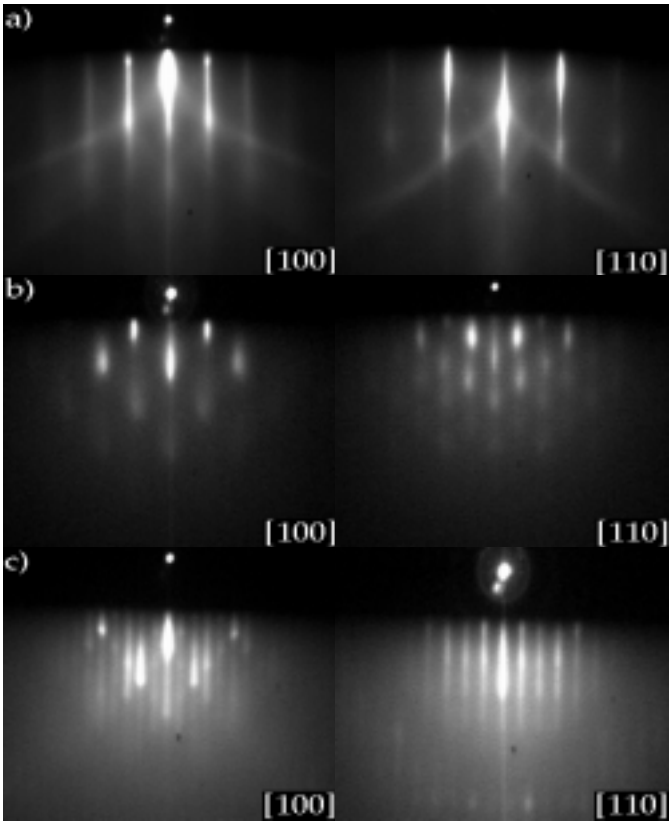

Fig. 5. RHEED patterns observed from Mn films grown at room temperature on a $Nb_{0.25}V_{0.75}(001)$ buffer layer: (a) up to 4 monolayer, (b) just above 4 ML, (c) thick deposit annealed at 450 K. A four-fold symmetry is observed in each case. The azimuths indicated on the RHEED patterns are given with respect to the buffer layer.

to the buffer layer diffraction peak. This means that the Mn out-of-plane lattice spacing is close to the buffer layer one. However, this is no more the case for relaxed Mn films (Fig. 7d), for which the superlattice peak is far from the buffer layer peak, and is no longer the most intense peak. Finally, this analysis shows that for the pseudomorphic regime, the in-plane pseudomorphism observed by RHEED also exists in the growth direction. Moreover, the relaxation above 4 Mn atomic planes observed by RHEED is confirmed by XRD. The out-of-plane parameter of the Mn pseudomorphic phase deduced from the XRD analysis is 2.94 ± 0.05 Å.

Because of its selective character, the EXAFS technique allows us to go further in the structure determination. The EXAFS analysis was performed on the three structures observed by RHEED (Figs. 8 and 9). For thick Mn films, the experimental EXAFS oscillations are compared to the simulated one using FEFF code assuming a Mnα structure. There is a good agreement between the experiment and the simulation, which confirms the epitaxy of Mnα on the $M_xV_{1-x}(001)$ lattices. Concerning the second relaxed structure observed for $x > 25\%$ and moderate thicknesses, the EXAFS analysis allows us to confirm that Mn is not in the well-known Mn structures, *i.e.* Mnα, Mnβ, fcc or bcc. However, we did not manage to identify this structure using FEFF. According to the Fourier transform of the EXAFS oscillations, we can only say that the number of first neighbours is small. This structure probably comes from the beginning of the relaxation to the Mnα structure.

Three typical sets of EXAFS oscillations obtained on superlattices where pseudomorphic Mn growth takes place are shown in Figure 9. The Mn EXAFS oscillations are almost similar for in-plane and out-of-plane polarization in Mn/V SLs, in contrast to Mn/Fe and Mn/NbV SLs for which the structure is no more cubic. The EXAFS spectra are well-fitted assuming a Mn bct with a c/a ratio close to 1. A similar analysis was performed on the corresponding Fe, Nb and V K-edge. The results are listed in Table 2. It should be noted that the lattice spacings deduced from the EXAFS analysis in the MV alloys' layers in the SLs are smaller than those measured by XRD on the thick MV buffer layers (see Fig. 3). This point can be simply understood by the fact that both Mn and MV layers are strained by each other in a superlattice. Such superlattice effects also explain the small differences between the lattice spacings determined here in Mn/V(001) SLs and on a single Mn layer grown on V(001) by Tian *et al.* [16]. However, despite this superlattice effect, our results are in agreement with [16]. This is an important point since the distances are not determined with the same technique in the two studies. Finally, as Tian *et al.* [16] cannot determine with confidence the original unstrained Mn phase which grows on V(001), the typical bcc-like EXAFS oscillations observed here on the Mn/V system definitely demonstrate that the corresponding Mn phase is very close to the bcc structure and cannot come from a distortion of any fcc structure.

At this stage of the investigation, it is natural to assume that these tetragonal structures come from a distortion of a unique bcc Mn structure, since the Mn structure is almost bcc on V. This point can be checked by using elastic theory. Assuming that Mn is only stressed in-plane, the in-plane and out-of-plane strains $\varepsilon_{\parallel}$ and $\varepsilon_{\perp}$ are related by the equation:

$$\varepsilon_{\perp} = \frac{a_{\perp} - a_0}{a_0} = -\left(\frac{2\nu}{1-\nu}\right)\varepsilon_{\parallel} = -\left(\frac{2\nu}{1-\nu}\right)\left(\frac{a_{\parallel} - a_0}{a_0}\right) \quad (4)$$

where ν is the Poisson ratio and a_0 the lattice spacing of the unstrained bcc Mn structure. As several sets of $a_{\parallel}$ and $a_{\perp}$ values are known, we can calculate by using equation (4) $a_0 = 2.92 \pm 0.03$ Å and $\nu = 0.30 \pm 0.03$ (Tab. 2).

In summary, the pseudomorphic Mn phases observed in Mn/Fe(001), $Mn/Fe_xV_{1-x}(001)$, and $Mn/Nb_xV_{1-x}(001)$ SLs are bct with a c/a ratio varying from 0.97 to 1.05. Moreover, the elastic analysis allows us to demonstrate that these Mn bct structures come from the same unstrained Mn phase, the bcc Mn phase, with a lattice spacing of 2.92 ± 0.03 Å and a Poisson ratio of 0.30 ± 0.03 at room temperature.

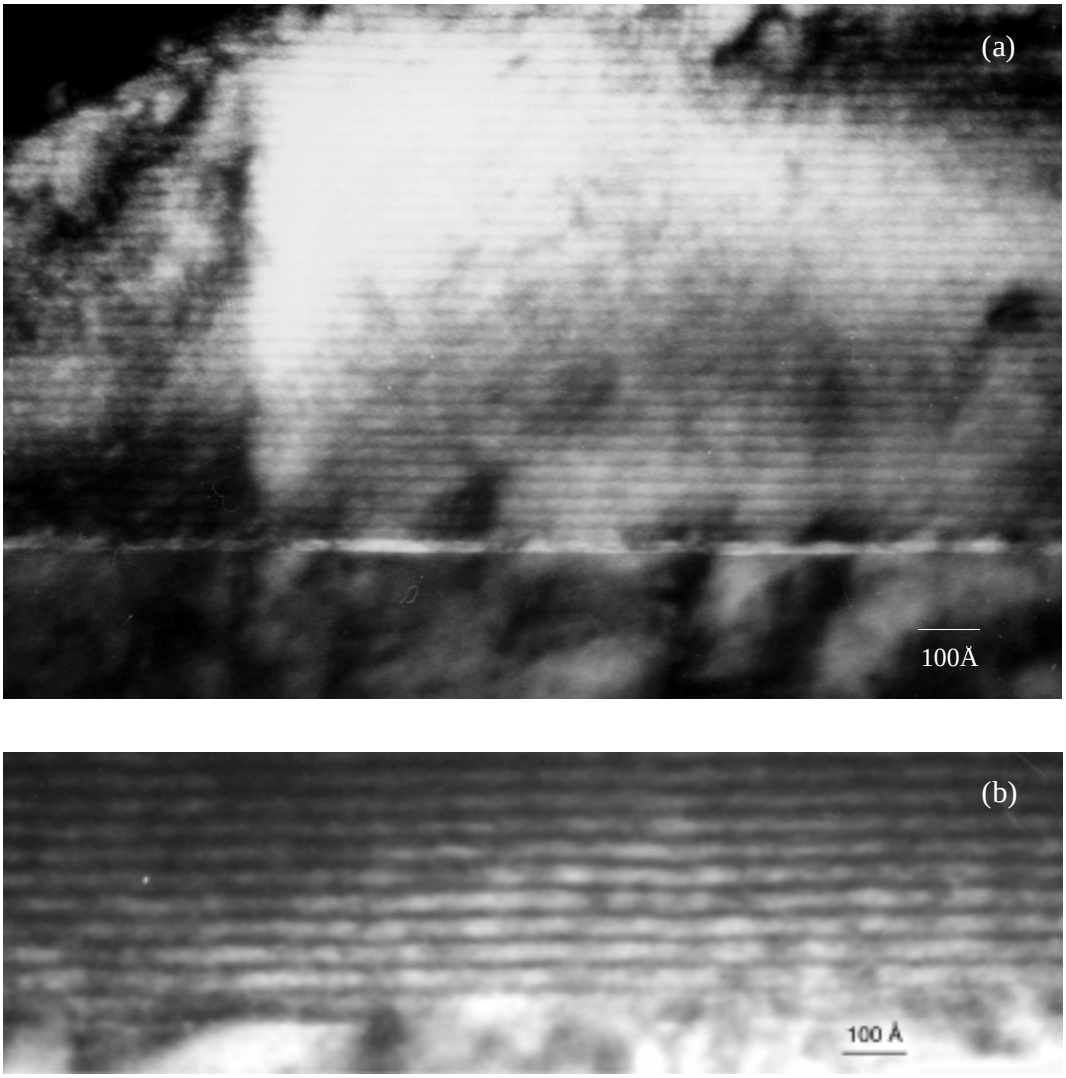

Fig. 6. Transmission electron microscopy images of two superlattices with the following stacking sequences: (a) (Mn(6 Å)/$Fe_{0.25}V_{0.75}$(17 Å)) and (b) (Mn(6 Å)/$Nb_{0.25}V_{0.75}$(24 Å)). In both images, the Mn layers are dark.

Table 2. M_xV_{1-x}, and Mn lattice spacings for a series of superlattices determined by the EXAFS analysis. The structure of the M_xV_{1-x} layers is bcc, although Mn is always found in a tetragonal structure. The last columns indicates the c/a ratio and the calculated values corresponding to the unstrained bcc Mn phase (given by Eq. (4)).

samples	M_xV_{1-x} $a(\pm 0.01$ Å)	Mn $a_{\parallel}(\pm 0.01$ Å)	Mn $a_{\perp}(\pm 0.02$ Å)	c/a (± 0.01)	a_0 (calc) (± 0.03 Å)
(Mn(9 Å)/Fe(15 Å)) × 30	Fe 2.86	2.85	2.98	1.05	2.92
(Mn(6 Å)/$Fe_{0.25}V_{0.75}$(18 Å)) × 100	Fe 2.92 V 2.92	2.92	2.88	0.99	2.90
(Mn(4.5 Å)/V(6 Å)) × 100	V 2.93	2.93	2.90	0.99	2.92
(Mn(6 Å)/V(12 Å)) × 75	V 2.94	2.95	2.89	0.98	2.92
(Mn(6 Å)/$Nb_{0.25}V_{0.75}$(24 Å)) × 100	V 2.99	2.98	2.88	0.97	2.93

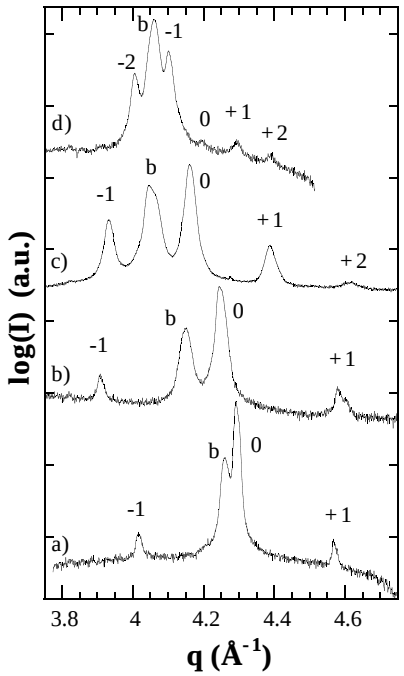

Fig. 7. X-ray diffraction diagrams in the $\theta - 2\theta$ mode for: (a) (Mn(6 Å)/$Fe_{0.25}V_{0.75}$(17 Å)) × 100 (TEM image a); (b) (Mn(6 Å)/V(12 Å)) × 75; (c) (Mn(6 Å)/$Nb_{0.25}V_{0.75}$(24 Å)) × 100 (TEM image b); (d) (Mn(30 Å)/$Nb_{0.25}V_{0.75}$(40 Å)) × 25 (b: peak from the buffer layer, −1, 0, +1: indexation of the SLs peaks).

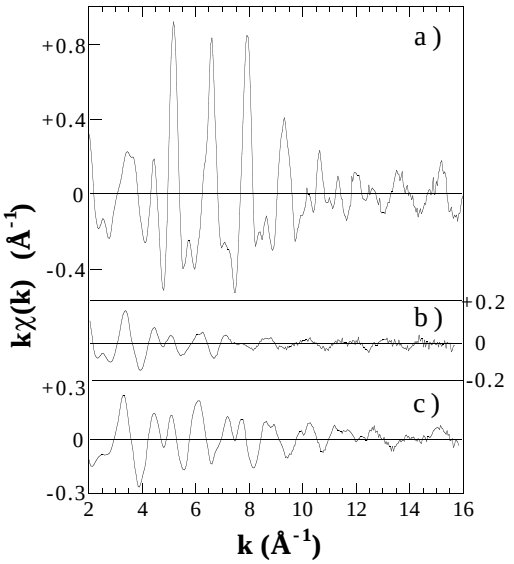

Fig. 8. EXAFS oscillations measured on three samples corresponding to the three Mn structures observed by RHEED: (a) (Mn(4.5 Å)/V(6 Å)) × 100 SL; (b) (Mn(30 Å)/$Nb_{0.25}V_{0.75}$(40 Å)) × 25 and (c) 900 Å thick Mn film grown on a $Nb_{0.5}V_{0.5}$ buffer layer. The EXAFS oscillations are isotropic in (b) and (c) and very similar for both X-ray polarizations in (a).

3.4 Magnetic properties

The macroscopic magnetic properties of Mn/MV superlattices were first examined using SQUID magnetometry. No magnetization was detected down to 4 K, with the applied magnetic field as large as 7 T. The corresponding strained bcc Mn phase was consequently not ferromagnetically ordered. A previous XMCD study performed on Mn/Fe(001) superlattices allowed us to show that Mn is also not in a ferromagnetic state in such samples, *i.e.* for Mn coated by Fe films.

However, the situation is different for uncoated Mn films grown on (001) Fe buffer layers. We actually observed a Mn ferromagnetic order up to two deposited atomic planes. Since this particular behaviour could also take place in the Mn/MV system, we performed XMCD measurements on uncoated Mn films grown on (001) V. The samples were prepared in a MBE chamber coupled to the UHV chamber where the XMCD measurements were performed (see Ref. [14] for more details). In contrast to uncoated Mn ultra-thin films on Fe(001), the XMCD signal is equal to zero for the two samples studied, *i.e.* 0.2 and 1 ML Mn/V(001) (Fig. 10), at room temperature but also down to 100 K, with applied magnetic fields as large as 1 T. This result can be interpreted as a lack of ferromagnetic order in the bcc Mn phase, but can also be due to oxygen contamination. Indeed, we have shown that the oxygen contamination of the Mn ultra-thin films grown on (001) Fe drastically influences the Mn magnetic properties. When the Mn films are not oxidized, ferromagnetic order takes place with a parallel Mn/Fe coupling. However, when the Mn films are totally oxidized (leading to MnO), a ferromagnetic order still exists in the Mn films but the Mn/Fe coupling is reversed. When the Mn films are nearly half-oxidized, the corresponding XMCD signal was shown to be close to zero. The XMCD signals coming from the oxidized and unoxidized parts of the Mn films thus exactly cancel each other. Such a scenario may also occur in the Mn/V(001) system. The oxygen contamination in the Mn/V(001) system must consequently be evaluated. However, and contrary to the Mn/Fe system, the oxygen quantity in the Mn/V(001) system cannot be easily determined by XPS since the O 1*s* peak is mixed with the V 2*p* peak, neither by AES since the KLL O and LMM V transitions also overlap in energy. We had consequently to find another way to determine the oxygen contamination and its possible influence on the Mn magnetic properties.

This goal can be achieved by analysing the ratio between the $2p^{3/2}$ and $2p^{1/2}$ Mn absorption peaks called here the branching ratio [20]. In the case of unoxidized Mn films grown on Fe(001), a BR close to 2 is observed. However, when the Mn film is totally oxidized, this BR rises to 3.2 [14]. Consequently, the BR determination is a good tool to determine the oxygen contamination. For the 0.2 ML Mn/V(001) sample studied here, a BR close to 2.5 ± 0.2 was measured, leading to an oxygen contamination near $40 \pm 15\%$ of the entire Mn layer. The lack of ferromagnetic ordering in this sample might thus be explained by an oxygen contamination. However, a BR equal to 2.0±0.1 was measured on the 1 ML Mn/V(001) sample, leading to an oxygen contamination between 0 and 10%.

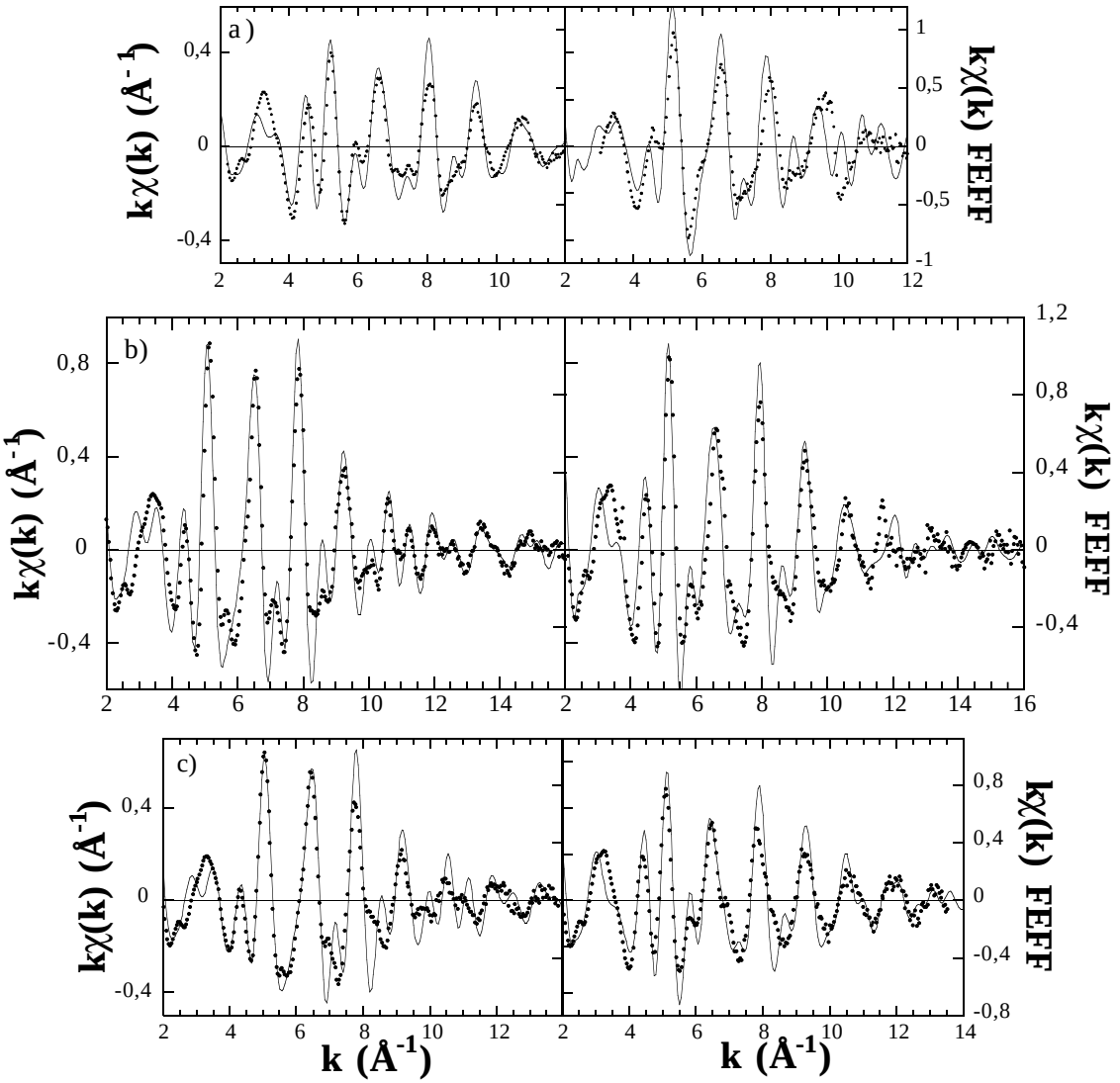

Fig. 9. EXAFS oscillations (points) and FEFF simulations (lines) for in-plane and out-of-plane polarizations for the three samples of Figures 7a–c, for which Mn is observed to be pseudomorphic to the corresponding MV alloy. The lattice spacing values of Table 2 are used for the simulations. For a better evaluation of the EXAFS dynamics from one sample to another, the same scale is respected for all the plots.

Such an oxygen quantity in the Mn layer cannot mask any possible Mn ferromagnetic ordering. We can consequently go as far as to say that no Mn ferromagnetic ordering takes place for 1 ML Mn/V(001) even down to 100 K.

In summary, except in the special case of uncoated ultra-thin Mn films grown on (001) Fe, no ferromagnetic order was observed in Mn/MV(001) superlattices for which the Mn structure is close to the bcc one. As the Mn critical thickness does not exceed four atomic planes on NbV and FeV alloys, one can argue that this lack of ferromagnetism may be the consequence of interfacial electronic exchange, particularly with V. However, this critical thickness is much larger on (001) Fe (10 atomic planes), leading to a small contribution due to the interfaces, and the Mn films are also not found to be in a ferromagnetic state above two atomic planes. We can consequently go as far as to say that bcc Mn, even strained, is neither stable in a ferromagnetic state, nor in a ferrimagnetic state as proposed in references [4,5], but probably in a antiferromagnetic state. This result is in agreement with the theoretical results of Elmhoussine *et al.* [6], who predict an antiferromagnetic ground state in bct Mn for the c/a range investigated here. Finally, this study shows that the ferromagnetic state observed in uncoated Mn films up to two atomic planes on (001) Fe has three origins: the Mn hybridization with Fe, the two-dimensional behaviour of the Mn films, and the broken symmetry due to the surface.

4 Conclusion

In this paper, we have shown that several Mn crystalline structures can be obtained on buffer layers made of bcc (001) alloys with a tunable lattice spacing. Mn is observed

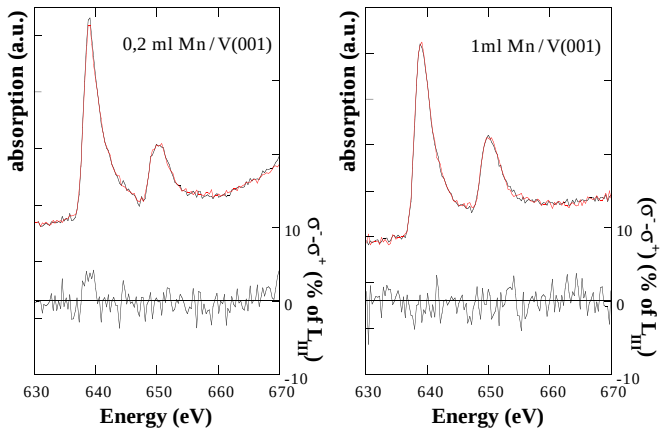

Fig. 10. L absorption spectra and XMCD signal observed on 0.2 ML (left) and 1 ML (right) thick Mn films epitaxially grown on (001) V. One can see that the $L_{\rm III}/L_{\rm II}$ ratio is higher on the 0.2 ML than on the 1 ML Mn film, which is an indication of an oxygen contamination in the 0.2 ML Mn film.

to be pseudomorphic to the (001) Fe up to 10 atomic planes, and to (001) Fe_xV_{1-x} and Nb_xV_{1-x} ($\leq 25\%$) up to 4 atomic planes. The EXAFS analysis shows that the corresponding structure is bct with a c/a ratio varying from 0.97 to 1.05, *i.e.* very close to the bcc structure. Moreover, the elastic theory allows us to demonstrate that all the Mn bct structures observed in the SLs derive from the distortion of a unique bcc Mn structure, characterized by a lattice spacing close to 2.92 Å, and a Poisson ration near 0.3 at room temperature. No ferromagnetic ordering was observed in the superlattices, but also in uncoated Mn films on (001) V. The only evidence of ferromagnetic ordering was observed in uncoated Mn ultra-thin films grown on (001) Fe. However, this former ferromagnetic state is due to the Mn/Fe hybridization, to the 2D magnetic behaviour, and to the presence of the surface. This is clearly not the ground magnetic state of the thicker strained bcc Mn films studied here.

References

1. For a review, see: H. Dreyssé, C. Demangeat, Surf. Sci. Rep. **28**, 65 (1997).
2. See for instance: M.T. Kief, W. Egelhoff, Phys. Rev. B **47**, 10785 (1993).
3. V.L. Moruzzi, P.M. Marcus, J. Kübler, Phys. Rev. B **39**, 6957 (1989).
4. V.L. Moruzzi, P.M. Marcus, Solid State Commun. **71**, 203 (1989).
5. S. Fujii, S. Ishida, S. Asano, J. Phys. Soc. Jpn **60**, 1193 (1991).
6. P. Krüger, O. Elmouhssine, C. Demangeat, J.C. Parlebas, Phys. Rev. B **54**, 6393 (1996).
7. B. Heinrich, A.S. Arrott, C. Liu, S.T. Purcell, J. Vac. Sci. Technol. A **5**, 1935 (1987).
8. Y. Nishihata, M. Nakayama, N. Sano, H. Teraushi, J. Appl. Phys. **63**, 319 (1988).
9. D. Tian, S.C. Wu, F. Jona, P.M. Marcus, Solid State Commun. **70**, 199 (1989).
10. W.F. Egelhoff, I. Jacob, J.M. Rudd, J.F. Cochan, B. Heinrich, J. Vac. Sci. Technol. **8**, 1582 (1990).
11. W.L. O'Brien, B.P. Tonner, Phys. Rev. B **50**, 2963 (1994).
12. K. Ounadjela, P. Vennègues, Y. Henry, A. Michel, V. Pierron-Bohnes, J. Arabski, Phys. Rev. B **49**, 8561 (1994).
13. S. Andrieu, H. Fischer, A. Traverse, M. Piecuch, Phys. Rev. B **54**, 2822 (1996).
14. S. Andrieu, M. Finazzi, F. Yubero, H. Fischer, P. Arcade, F. Chevrier, L. Hennet, K. Hricovini, G. Krill, M. Piecuch, Europhys. Lett. **38**, 459 (1997); S. Andrieu, M. Finazzi, Ph. Bauer, H. Fischer, P. Lefevre, A. Traverse, K. Hricovini, G. Krill, M. Piecuch, Phys. Rev. B **57**, 1985 (1998).
15. S.K. Kim, Y. Tian, M. Montesano, F. Jona, P.M. Marcus, Phys. Rev. B **54**, 5081 (1996).
16. Y. Tian, F. Jona, P.M. Marcus, Phys. Rev. B **59**, 12647 (1999).
17. See for instance: *Low energy electrons and surface chemistry*, edited by G. Ertl, J. Küppers (VCH publishers, 1985).
18. J.H. Scofield, J. Electr. Spectr. **8**, 129 (1976).
19. B. Kierren, T. Gourieux, F. Bertran, G. Krill, Appl. Surf. Sci. **68**, 341 (1993); C. Sürgers, H.V. Löhneysen, Appl. Phys. A **54**, 350 (1992).
20. The correct definition of the Branching Ratio is the ratio $I_{\rm LIII}/(I_{\rm LII}+I_{\rm LIII})$. We define it here as $I_{\rm LIII}/I_{\rm LII}$ for convenience.